



## Use of cobalt ferrite and activated carbon in supercapacitors

Daysianne Kessy Mendes Isidorio<sup>1,\*</sup>, Érick A. Santos<sup>2</sup>, Arquimedes Lopes Nunes Filho<sup>1</sup>, Pedro Henrique Poubel Mendonça da Silveira<sup>1</sup>, Amal Elzubair Eltom<sup>1</sup>, Ronaldo Sergio de Biasi<sup>1</sup>

<sup>1</sup>Military Institute of Engineering, Materials Science Program, Praça General Tibúrcio 80, Rio de Janeiro, RJ, 22290-270, Brazil

<sup>2</sup>Advanced Energy Storage Division, Center for Innovation on New Energies, University of Campinas, Av. Albert Einstein 400, Campinas, SP, 13083-852, Brazil

Received 21 February 2022; Received in revised form 30 June 2022; Received in revised form 20 October 2022; Accepted 22 November 2022

### Abstract

Supercapacitors are energy storage devices that can cleanly and efficiently meet the growing energy demand. The present work describes the synthesis of nanoparticles of cobalt ferrite ( $\text{CoFe}_2\text{O}_4$ ) by the combustion method and their use with activated carbon (AC) to manufacture supercapacitors. In order to study the influence of composition on the electrochemical properties, supercapacitors with three different compositions were produced: Fe90 (90%  $\text{CoFe}_2\text{O}_4$  and 10% AC), Fe50 (50%  $\text{CoFe}_2\text{O}_4$  and 50% AC) and Fe10 (10%  $\text{CoFe}_2\text{O}_4$  and 90% AC). Microstructural and morphological analyses were performed by X-ray diffraction (XRD), scanning electron microscopy (SEM), transmission electron microscopy (TEM), and Raman spectroscopy. Cyclic voltammetry (CV), galvanostatic charge-discharge (GCD), floating and electrochemical impedance spectroscopy (EIS) tests were performed. XRD, SEM, TEM and Raman results showed that the combustion method was effective for the production of  $\text{CoFe}_2\text{O}_4$  nanoparticles. SEM and Raman spectroscopy results showed that the AC has a porous structure and low crystallinity. According to CV, GCD and floating tests, all three supercapacitors presented excellent electrochemical stability. The Fe50 composition yielded the lowest equivalent series resistance, while the Fe10 composition yielded the highest capacitance. The results show that the combination of AC with  $\text{CoFe}_2\text{O}_4$  is promising for the use in supercapacitors.

**Keywords:** supercapacitors, cobalt ferrite, activated carbon, energy storage

### I. Introduction

The long-term harmful effects of greenhouse gases in the atmosphere and the rapid depletion of fossil resources lead to the need to explore renewable energy resources and new devices for energy generation and storage [1]. Supercapacitors or electrochemical capacitors are promising energy storage devices to meet this demand since they have high specific capacitance, fast charge/discharge rate and long cycles [2,3].

According to the electrical charge storage mechanism, supercapacitors can be divided into three categories: double-layer electrochemical capacitors (EDLCs), pseudocapacitors and hybrid capacitors. In

EDLCs, the capacitance occurs by the accumulation of electrostatic charges at the interface between the electrodes and the electrolyte; thus, the capacitance is directly proportional to the surface area of the electrodes [1]. In pseudocapacitors, energy storage arises from fast reversible oxi-redox reactions at the interface between the electrode and the electrolyte [4]. Energy storage in hybrid supercapacitors occurs by a combination of the two processes [5]. The most common materials used in EDLC supercapacitors are carbon-based materials (e.g. activated carbon [6] and graphene [7]), metal oxides (e.g.  $\text{RuO}_2$  [8],  $\text{NiO}$  [9],  $\text{MnO}_2$  [10]) and conducting polymers, such as polyaniline [11].

Activated carbon (AC) is frequently used in EDLCs due to its high surface area (up to  $3000 \text{ m}^2/\text{g}$ ), high electrical conductivity and low cost. Although AC supercapacitors have a high power density, their small specific

\*Corresponding author: tel: +55 21 99099 7006  
e-mail: [daysiannekessy@ime.eb.br](mailto:daysiannekessy@ime.eb.br)

capacitance is a drawback for many applications. Cobalt ferrite ( $\text{CoFe}_2\text{O}_4$ ) has been suggested for use in pseudosupercapacitors due to its multivalent oxidation, high theoretical specific capacitance and electrochemical stability [12–18]. However, pure  $\text{CoFe}_2\text{O}_4$  does not yield a satisfactory performance due to its low power density, so the approach of making AC/ $\text{CoFe}_2\text{O}_4$  hybrids may provide good results [19,20].

In this work, we synthesized supercapacitors based on activated carbon and  $\text{CoFe}_2\text{O}_4$  with different compositions. The electrochemical properties were evaluated and correlated to the material structure. The results showed that the supercapacitors have excellent electrochemical stability and good capacitance.

## II. Experimental

### 2.1. Supercapacitor preparation

The starting materials were cobalt nitrate ( $\text{Co}(\text{NO}_3)_2 \cdot 6\text{H}_2\text{O}$ , Alphatec), iron nitrate ( $\text{Fe}(\text{NO}_3)_3 \cdot 9\text{H}_2\text{O}$ , CRQ Produtos Químicos), glycine ( $\text{C}_2\text{H}_5\text{NO}_2$ , Sigma Aldrich), polyvinylidene difluoride (PVDF, Sigma Aldrich, molecular weight 534), N-methyl-2-pyrrolidinone (NMP, Sigma Aldrich) and activated carbon (NORIT® SX Plus CAT, Sigma Aldrich).

To produce 1 g of cobalt ferrite powder, cobalt nitrate and iron nitrate, in a ratio of 1:2, were dissolved in 10 ml of distilled water. The fuel was glycine, with a glycine/nitrate molar ratio of 1:1. The mixture was stirred until a homogeneous solution was obtained. The solution was kept in a hot plate at  $100^\circ\text{C}$  until combustion occurred after approximately 20 min. The resulting powder was macerated in a mortar.

The first step in preparation of supercapacitor was mixing of 80% active material ( $\text{CoFe}_2\text{O}_4 + \text{AC}$ ), 10% polyvinylidene fluoride (PVDF) and 10% conductive additive (Tob New Energy brand, code T-SUP). Three different compositions were prepared and named Fe10 (10%  $\text{CoFe}_2\text{O}_4$  and 90% AC), Fe50 (50%  $\text{CoFe}_2\text{O}_4$  and 50% AC) and Fe90 (90%  $\text{CoFe}_2\text{O}_4$  and 10% AC). PVDF is a highly non-reactive thermoplastic fluoropolymer that is used for the synthesis of carbonaceous electrodes of supercapacitors as a binder compound, and the conductive additive is a very high purity carbon widely used in lithium battery production. As solvent, 1 ml of methylpyrrolidone (NMP) was added to each 100 mg of active material. This mixture was kept under magnetic stirring for 15 min and then it was taken to an ultrasonicator for 15 min.

To manufacture the electrodes,  $60\ \mu\text{l}$  of the mixture were deposited on Ni foil substrates with 10 mm diameter as shown in Fig. 1, and then taken to a hot plate for 2 h. The electrodes were placed in an oven at  $60^\circ\text{C}$  for 12 h to remove the solvent. A cellulose paper, NKK brand TF4850, was used as a separator and 6 M aqueous solution of KOH for the electrolyte. The supercapacitors were manufactured in a symmetrical configuration using the 2032-coin cell model.

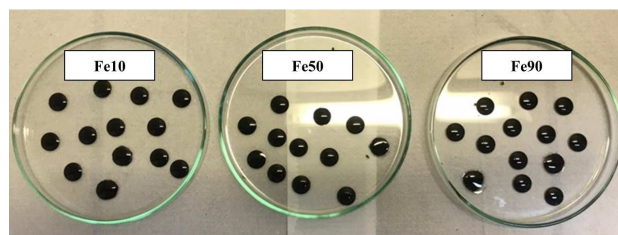


Figure 1. Electrodes with different compositions

Figure 2 shows each component of the supercapacitor. The components were arranged as follows: a conical spacer, a stainless steel current collector, an electrode and a separator were placed inside of a metallic capsule. Then,  $60\ \mu\text{l}$  of electrolyte were dropped in the separator. After that the counter electrode, the current collector and the negative part of the metallic capsule were placed in the capsule. Finally, for sealing and consolidating the supercapacitor, a pressure of 6.9 MPa (1000 psi) was applied using a TOB GN-110 hydraulic press.

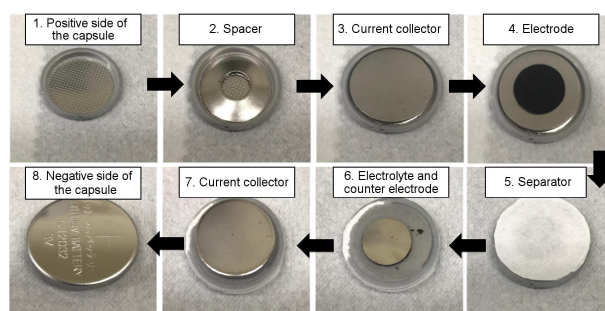


Figure 2. Components of the supercapacitor

### 2.2. Characterization

The crystal structures of  $\text{CoFe}_2\text{O}_4$  and AC were determined by X-ray diffractometry (XRD) using a Shimadzu XRD-7000 diffractometer equipped with a  $\text{Co-K}\alpha_1$  ( $\lambda = 0.179\ \text{nm}$ ) radiation source, using a step size of  $0.05^\circ$  and dwell time of  $150\ \text{s}/^\circ$ . The crystallite size and lattice parameters of the samples were determined from XRD data by the Rietveld refinement.

Morphological and microstructural analyses were performed by field emission scanning electron microscopy (FESEM) using a QUANTA FEG 250 system and transmission electron microscopy (TEM), using a JEOL JEM 1200EX-II system. Raman spectra were recorded using a 514.5 nm argon-ion laser on a Renishaw spectrophotometer.

In a two-electrode configuration, electrochemical measurements were carried out with 6 M KOH as electrolyte. Electrochemical characterization using cyclic voltammetry (CV), galvanostatic charge/discharge (GCD), chronoamperometry (CA), and electrochemical impedance spectroscopy (EIS) were performed in a Biologic SP-200 potentiostat-galvanostat. The CV and GCD measurements were conducted in the potential range of 0.8 to 1.1 V. The GCD tests were performed using a gravimetric current of  $0.75\ \text{mA/g}$  and charging

and discharging the supercapacitors up to a voltage of 1 V. In the floating test, the supercapacitors under a constant voltage of 1 V went through 10 ageing cycles of 12 h. At the end of each cycle, GCD electrochemical test was performed to assess the capacitance retention of the device. The study of ion transport and conductivity of electroactive materials was carried out by EIS performed in a frequency range from 10 mHz to 10 kHz, with 10 points per decade and 10 mV amplitude using DC voltage signal from 0.8 to 1.1 V. From the GCD, the specific capacitance ( $C_s$ ) was calculated using the following equation [21]:

$$C_s = \frac{i \cdot \Delta t}{\Delta U \cdot m} \quad (1)$$

where  $i$  is the current density,  $\Delta t$  is the discharge time,  $\Delta U$  is the potential drop during discharge and  $m$  is the supercapacitor mass. The specific energy ( $E$ ) was calculated using Eq. 2:

$$E_s = \frac{C_s \cdot \Delta U^2}{2} \quad (2)$$

The specific power ( $P$ ) was calculated using Eq. 3:

$$P_s = \frac{E}{t} \quad (3)$$

where  $t$  is the discharge time. The equivalent resistance ( $R_{ESR}$ ) was calculated using Eq. 4:

$$R_{ESR} = \frac{\Delta U}{2i} \quad (4)$$

### III. Results and discussion

#### 3.1. Morphological and structural characterizations

X-ray diffraction patterns of the  $\text{CoFe}_2\text{O}_4$  and AC are shown in Fig. 3. The Rietveld refinement was performed with the aid of Fullprof program. The refinement of the  $\text{CoFe}_2\text{O}_4$  synthesized by combustion method is shown in Fig. 3a, where the pink, black and blue colours

represent the experimental points, the fitted profile and the difference between the observed and calculated profiles, respectively. The diffraction peaks in the  $2\theta$  range of  $10\text{--}55^\circ$  correspond to the characteristic reflections of the cubic spinel structure, space group  $Fd\bar{3}m$  (No. 227) [22]. The diffraction patterns and the relative intensity of all diffraction peaks match well with the standard card JCPDS 022-1086, supporting the formation of  $\text{CoFe}_2\text{O}_4$  phase [23]. The value of lattice parameter of  $\text{CoFe}_2\text{O}_4$  is  $8.487 \text{ \AA}$ , in reasonable agreement with other values reported [24,25,28]. The crystallite size was found to be 41 nm, similar as in other studies [24–26]. Figure 3b shows the AC XRD pattern. There are two very broad peaks centred at approximately  $2\theta = 25^\circ$  and  $50^\circ$  corresponding respectively to the diffraction of the graphitic basal plane (002) and the characteristic of the  $sp^3$ -hybridized lattice reflections (100) [13,29–31]. These large widths of the AC diffraction pattern indicate an amorphous and disordered nature of the AC [13, 30–33].

Figure 4 shows Raman spectra of the  $\text{CoFe}_2\text{O}_4$  and AC. For the  $\text{CoFe}_2\text{O}_4$ , the vibrational modes observed at  $308, 470, 575, 624$  and  $680 \text{ cm}^{-1}$ , as shown in Fig. 4a, are attributed to the vibrational modes  $T_{2g(1)}, E_g, T_{2g(2)}, T_{2g(3)}$  and  $A_{1g}$  [34,35]. In Fig. 4b, four bands, located at  $1188, 1340, 1535$  and  $1599 \text{ cm}^{-1}$ , were observed, which correspond to bands D1, D, D2 and G, respectively [16,36]. The two main bands are D and G: the D band is related to crystal lattice defects involving a double resonance process in the Brillouin zone and the G band is associated with the graphitized material, which has  $sp^2$  planar bonds between carbons due to  $E_{2g}$  Raman vibration mode. D1 and D2 bands are assigned to amorphous domains associated with  $sp^2$  clusters of four-fold coordinated bonds. The high intensity of the D band suggests that the carbonaceous material has a high defect density. The amorphous structure of the material can be estimated from the intensity ratio between the D and G bands ( $I_D/I_G$ ): the higher the ratio, the greater the degree of disorder. The calculated  $I_D/I_G$  value based on Fig. 4b was 1.11, which indicates low crystallinity of the AC.

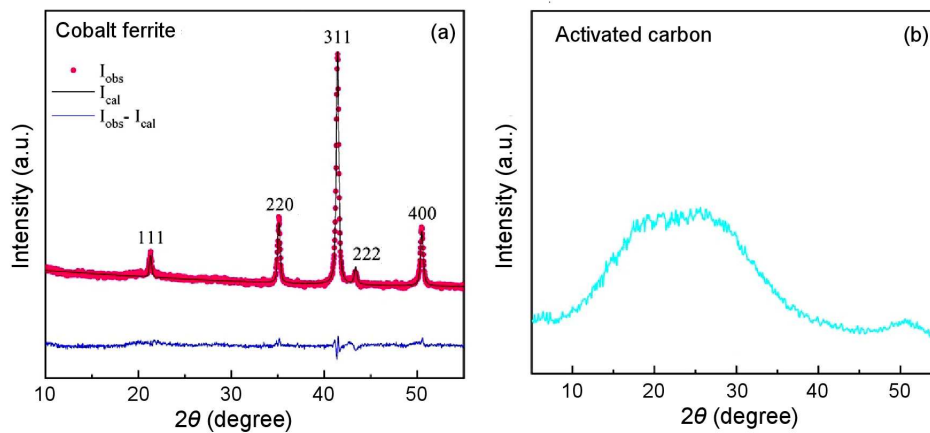


Figure 3. XRD patterns of: a)  $\text{CoFe}_2\text{O}_4$  and b) AC

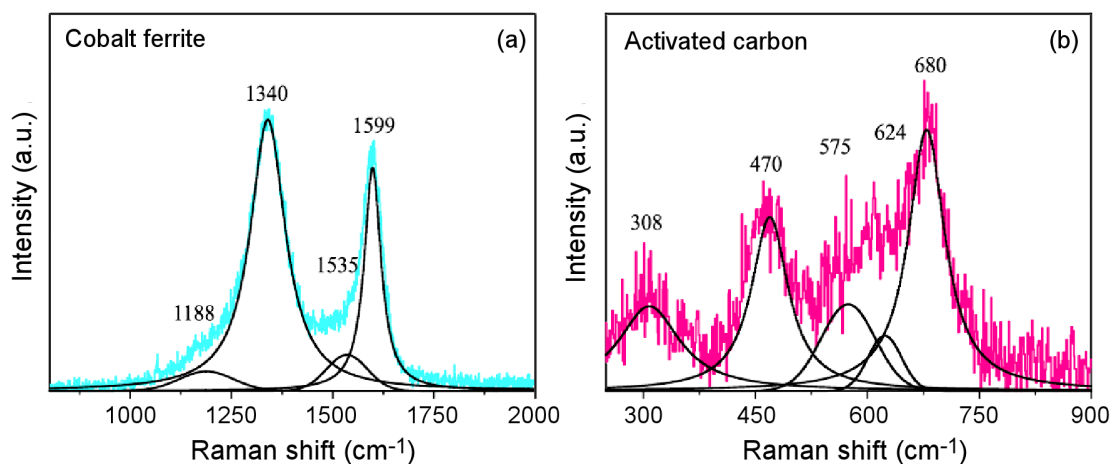


Figure 4. Raman spectra of: a)  $\text{CoFe}_2\text{O}_4$  and b) AC

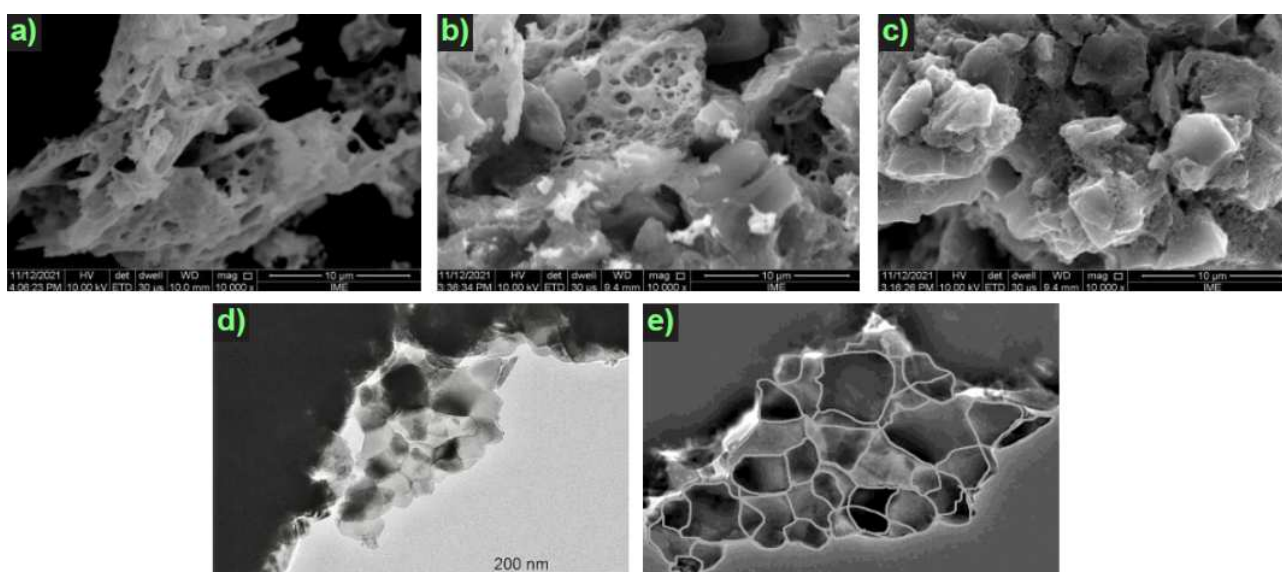


Figure 5. SEM images of: a) Fe10, b) Fe50 and c) Fe90; TEM image of  $\text{CoFe}_2\text{O}_4$  (d); delimitation of the nanoparticles of TEM image by ImageJ (e)

Figures 5a-c show the morphology of the supercapacitors Fe10, Fe50 and Fe90. Figures 5a,b present a structure rich in pores related to the low number of the  $\text{CoFe}_2\text{O}_4$  particles deposited in the AC cavities. These open channels may improve the contact of the electrolyte/electrode interface and thus enhance the diffusion of the electrolyte ions. Figure 5c of the Fe90 shows much less porosity than other samples (Fe10 and Fe50) indicating that the AC pores were clogged with  $\text{CoFe}_2\text{O}_4$  agglomerates. The low porosity of the Fe90 impairs electrolyte mobility, leading to low capacitance and high resistance.

TEM image of the  $\text{CoFe}_2\text{O}_4$  nanoparticles is shown in Fig. 5d and, similarly to a “bunch of grapes”, several isolated particles of  $\text{CoFe}_2\text{O}_4$  can be seen. With that low agglomeration, it is possible to observe the shape of the nanoparticles and their well-defined grain boundaries. From this image, the average size obtained by counting 64 nanoparticles was approximately 46 nm using ImageJ software to delimit the grain boundaries, Fig. 5e.

### 3.2. Electrochemical measurements

Figures 6a-c show the cyclic voltammograms of the Fe90, Fe50 and Fe10 supercapacitors measured at 10 mV/s in a potential range from 0.8 to 1.1 V. From the quasi-rectangular shape and cycle area of the voltammograms, the  $\text{CoFe}_2\text{O}_4$  and AC are good materials to be used in electrodes for potentials lower than 0.9 V in a 6 M KOH electrolyte [12]. The highest electrical current response was for the Fe10, followed by the Fe50 and with a much smaller value for the Fe90 supercapacitor. The obtained current is the combination of faradaic and capacitive current [19,37,38]. The area under the CV curve and the current plateau for the Fe10 are larger than those of the other supercapacitors leading to the highest capacitance, which is corroborated by GCD profiles. From Figs. 6a-c, it is verified that the supercapacitor Fe90 with the highest percentage of  $\text{CoFe}_2\text{O}_4$  is the one with a steeper slope at anodic vertex voltage of the voltammogram curve with potential above 0.9 V, indicating oxygen evolution reactions [1].

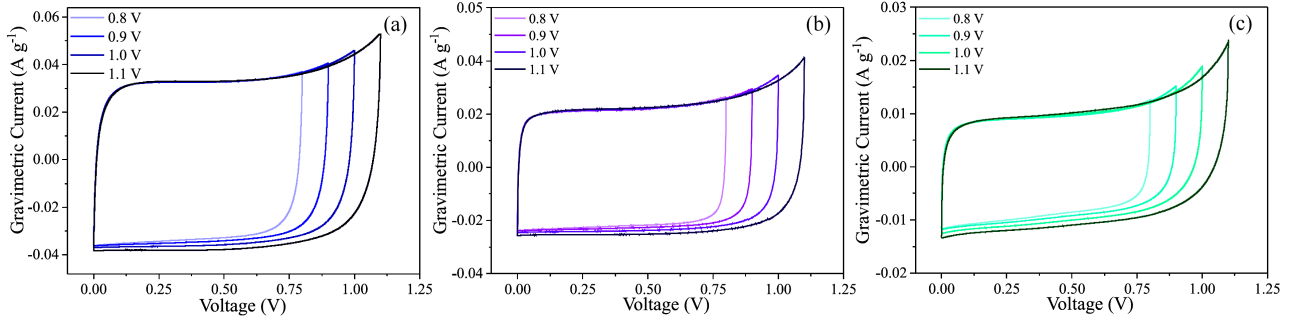


Figure 6. CV curves of: a) Fe10, b) Fe50 and c) Fe90

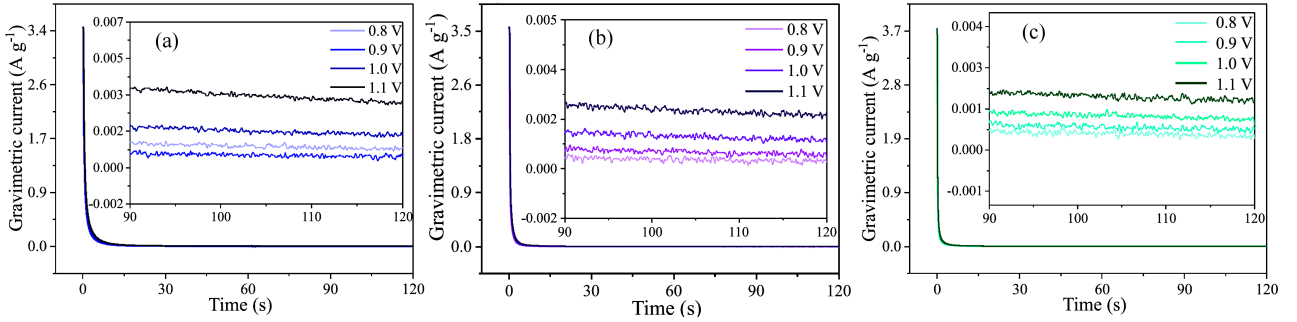
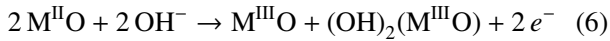


Figure 7. Chronoamperometry curves of: a) Fe10, b) Fe50 and c) Fe90

Although the CV curves do not show current peaks due to the faradaic  $\text{CoFe}_2\text{O}_4$  reactions, from the quasi-rectangular shape it is possible to estimate the influence of the ferrite on the faradaic reaction corresponding to different oxidation states of a metal according to Eqs. 5 and 6 [38]:



where M represents Fe or Co [13]. In a two-electrode well-behaved supercapacitor, the more rectangular the voltammogram curve is, the greater the electrochemical stability of the supercapacitor is. The electric current ( $I_C$ ) of a supercapacitor can be calculated using Eq. 7:

$$I_C = C_{EDL} \cdot \nu \left[ 1 - \exp\left(\frac{-\Delta U}{R_{ESR} \cdot C_{EDL} \cdot \nu}\right) \right] \quad (7)$$

where  $\nu$  is the voltage scan rate and  $\Delta U$  is the working voltage window (VWV). Thus, the  $I$  versus  $\nu$  plot for an ideal supercapacitor is expected to be a straight line. When the voltammogram curve after reaching the current plateau is slanted at the ends (vertices), this is an indication of electrolyte degradation: the oxygen evolution reactions (OER) and hydrogen evolution reactions (HER) gases from oxi-redox reactions lead to a current increase. An increase in the right extreme vertex in the voltammogram is due to OER, and in the left is due to HER. So, to evaluate this behaviour another model should be considered. The Butler-Volmer model takes into consideration the current increase at the voltammogram vertex due to a gas evolution [39]. The total cur-

rent ( $I$ ) is the sum of capacitive current ( $I_C$ ) and the OER faradaic current ( $I_{F(OER)}$ ), given by Eq. 8:

$$I = I_C + I_{F(OER)} = I_C + I_{0(a)} \exp\left(\frac{\alpha_a \cdot F(U - U_{0(OER)})}{R \cdot T}\right) \quad (8)$$

where  $\alpha_a$ ,  $R$ ,  $T$  and  $I_{0(a)}$ , are the anodic charge-transfer coefficient, the universal gas constant, the absolute temperature and the anodic exchange current density measured at  $U = U_{0(OER)}$ , respectively. Since the HER faradaic current ( $I_{F(HER)}$ ) is not taken into account in a two-electrode system, because the potentiostat considers only the working electrode signal, the phenomenon is not investigated in detail in this work. According to Eq. 8, the CV plots (Figs. 6a-c), and the chronoamperometry results (Figs. 7a-c), the OER currents increase  $\approx 50\%$  for a voltage of 0.9 V.

Figures 8a-c show GCD curves for the three supercapacitors exhibiting an almost triangular profile, characteristic of an EDLC behaviour also indicative of pseudocapacitive behaviour that was caused by a synergistic effect between  $\text{CoFe}_2\text{O}_4$  and AC [16,40]. This profile indicates good reversibility for the supercapacitors. The linearity and deviation in the GCD curves refer to the contribution of, respectively, EDLC and pseudocapacitance [5,19].

According to GCD tests at a current density of 0.1 A/g, the specific capacitances ( $C_s$ ) calculated for the Fe10, Fe50 and Fe90 supercapacitors were 14, 8 and 3 F/g, respectively. As the  $\text{CoFe}_2\text{O}_4$  concentration increases, the charge and discharge times decrease and the capacitance decreases. The capacitance was expected to increase when decorating the AC electrode with  $\text{CoFe}_2\text{O}_4$  nanoparticles, since the capacitance would

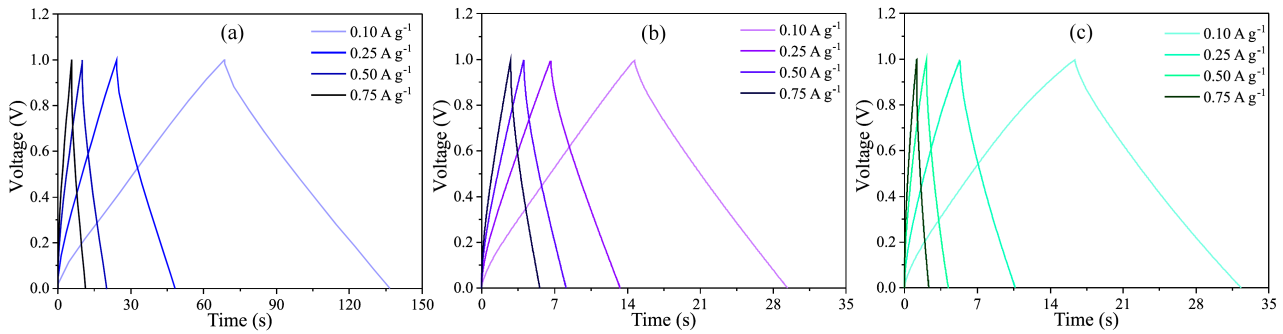


Figure 8. GCD curves of: a) Fe10, b) Fe50 and c) Fe90

be formed by two different and non-competing mechanisms: a purely physical EDLC mechanism from AC and a faradaic mechanism from the ferrite. A possible explanation for the fact that this did not happen is that the presence of narrow pores in the  $\text{CoFe}_2\text{O}_4$  structure, as seen in Fig. 6a, causes kinetic polarization, reducing the specific capacitance [41]. Furthermore, perhaps the method of preparation or the amount of material adopted was not ideal, so it is suggested that future works optimize the synthesis parameters of such supercapacitors to obtain optimal electrochemical properties.

The  $R_{ESR}$  values were determined from GCD results in Figs. 8a-c. The Fe50 achieved the lowest  $R_{ESR}$  value,  $0.80 \Omega$ . This low resistance reveals good conductivity of the electrode materials. A low  $R_{ESR}$  allows the supercapacitor to have a good diffusional flux for the formation of the EDLC [42]. Although the Fe50 has the lowest  $R_{ESR}$ , its capacitance was not the highest among the supercapacitors, as shown by the GCD results. The capacitive mechanism is more complex and not only dependent on the material's  $R_{ESR}$ , but also on other factors such as the surface porosity, type of pore, the interaction between support (carbon) and nanoparticles, etc. [15]. The Fe90 and Fe10 supercapacitors had higher  $R_s$  values,  $1.50$  and  $1.16 \Omega$ , respectively. One possible reason is that these devices do not have a good dispersion of particles in the porous structure. This hinders the ionic diffusion of the electrolyte on the electrode surface.

The GCD test can be used to determine the cyclic stability or coulombic efficiency ( $\eta$ ), given by the percentage ratio between the time of discharge and charge

of the devices. According to Fig. 9a, all supercapacitors showed excellent performance higher than 98% of the initial capacitance, indicating high capacitance retention. This behaviour can be attributed to the efficient ionic accessibility in the superficial pores of the electrode and by the chemical stability that cobalt ferrite presents [43].

As to electrochemical stability, Fig. 9b shows the capacitance retention for 120 h period under a floating test. Although the Fe50 and Fe90 do not have the highest CS, they showed capacitance retention greater than 106% of the initial values: the electrodes suffered no degradation, showing good stability when being potentially charging and discharging. According to Fig. 9b, there is an increase of the capacitance in the beginning of the test. This can be explained by the fact that initially the material is not fully used; by the time the whole AC and  $\text{CoFe}_2\text{O}_4$  structure is in contact with the electrolyte, the capacitance is larger [5]. The lowest capacitance retention was by the Fe10 supercapacitor, even though it can still be considered good, as it showed 99% of the initial capacitance. As the excellent cycle stability indicates, the  $\text{CoFe}_2\text{O}_4$  content improves the electrochemical stability [18].

For EIS analysis, Figs. 10a-c present the Nyquist diagrams which show two regions, a semicircle and vertical line, at high and low frequency regions, respectively. The values of charge transfer resistance ( $RCT$ ) for the Fe10, Fe50 and Fe90 are  $2.43$ ,  $1.64$  and  $3.66 \Omega$ , respectively. There are no significant changes in  $RCT$  for all supercapacitors at different potentials, what indi-

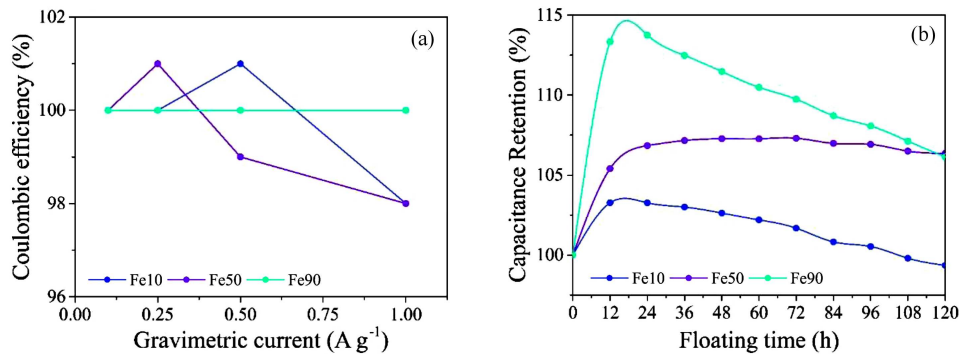


Figure 9. Coulombic efficiency of the supercapacitor at different gravimetric currents (a) and floating test with potential at 1 V (b)

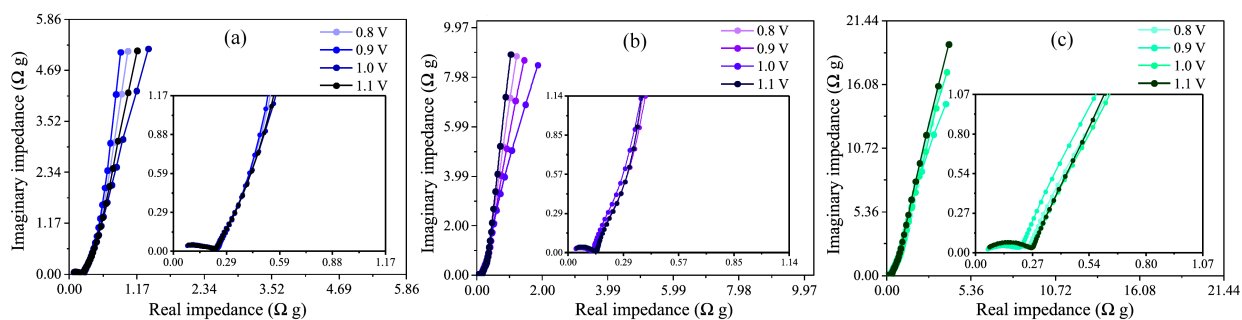


Figure 10. The Nyquist plots of: a) Fe10, b) Fe50 and c) Fe90

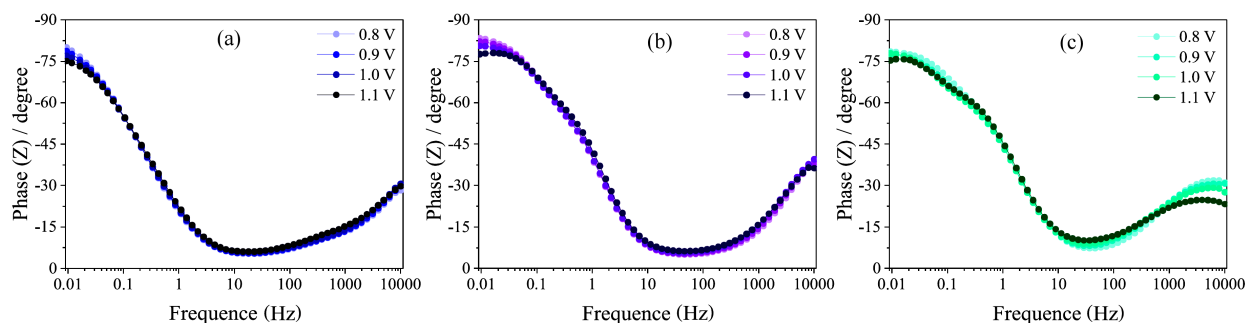


Figure 11. Bode plots of: a) Fe10, b) Fe50 and c) Fe90

icates that the semicircle formation is related to the supercapacitor impedance [44].

The Bode plots are displayed in Fig. 11. In the low frequency region, the prepared supercapacitors exhibited phase angles between  $75^\circ$  and  $82^\circ$ , similar to the results presented in the literature [45,46]. The Fe50 is the supercapacitor that presents an angle closer to  $90^\circ$ . The closer to  $90^\circ$  the phase angle is at low frequency, the closer a supercapacitor is to behaving as an ideal capacitor [15]. As it can be seen, the increase in potential within the window (0.8–1.1 V) causes the emergence of residual currents and the result shown in Fig. 7 was below 1%, which means that there was no degradation of the electrolyte.

#### IV. Conclusions

The preparation of  $\text{CoFe}_2\text{O}_4$  nanoparticles by the combustion method was confirmed by XRD, FESEM, TEM and Raman spectroscopy. Supercapacitors based on AC and  $\text{CoFe}_2\text{O}_4$  were produced in three compositions: Fe10, Fe50 and Fe90. The Fe10 supercapacitor showed the highest specific capacitance (8.52 F/g) and the lowest capacitance is that of the Fe90 (1.74 F/g) for a current of 0.75 mA/g. The smallest value of  $R_{ESR}$  was  $0.80 \Omega$  for the Fe50 supercapacitor. The supercapacitors Fe10 and Fe90 showed higher values of  $R_{ESR}$ ,  $1.16 \Omega$  and  $1.50 \Omega$ , respectively. The Fe50 supercapacitor presented a better balance between electrochemical stability and capacitive properties in comparison to other two samples. All supercapacitors showed excellent capacitance retention and coulombic efficiency. Thus, the  $\text{CoFe}_2\text{O}_4/\text{AC}$  materials showed to be very good candidates to be used in hybrid supercapacitors.

**Acknowledgment:** The authors thank the Brazilian funding agencies CAPES, FAPERJ, and FAPESP for financial support.

#### References

1. S. Zhang, N. Pan, "Supercapacitors performance evaluation", *Adv. Energy Mater.*, **5** (2015) 19–37.
2. P. Butnoi, A. Pangon, R. Berger, H.J. Butt, V. Intasanta, "Electrospun nanocomposite fibers from lignin and iron oxide as supercapacitor material", *J. Mater. Res. Technol.*, **12** (2021) 2153–2167.
3. R.R. Palem, S. Ramesh, H.M. Yadav, J.H. Kim, A. Sivasamy, H.S. Kim, J.H. Kim, S.H. Lee, T.J. Kang, "Nanostructured  $\text{Fe}_2\text{O}_3$ @nitrogen-doped multi-walled nanotube/cellulose nanocrystal composite material electrodes for high-performance supercapacitor applications", *J. Mater. Res. Technol.*, **9** (2020) 7615–7627.
4. Z. Gao, J. Wang, Z. Li, W. Yang, B. Wang, M. Hou, Y. He, Q. Liu, T. Mann, P. Yang, M. Zhang, L. Liu, "Graphene nanosheet/ $\text{Ni}^{2+}/\text{Al}^{3+}$  layered double-hydroxide composite as a novel electrode for a supercapacitor", *Chem. Mater.*, **23** (2011) 3509–3516.
5. S. Kumar, S. Sekar, A.K. Kalamurthy, S. Lee S, "Bifunctional rGO-NiCo<sub>2</sub>S<sub>4</sub> MOF hybrid with high electrochemical and catalytic activity for supercapacitor and nitroarene reduction", *J. Mater. Res. Technol.*, **12** (2021) 2489–2501.
6. E.Y.L. Teo, L. Muniandy, E.P. Ng, F. Adam, A.R. Mohamed, R. Jose, K.F. Chong, "High surface area activated carbon from rice husk as a high performance supercapacitor electrode", *Electrochim. Acta*, **192** (2016) 110–119.
7. S. Martinez-Vargas, A.I. Mtz-Enriquez, H. Flores-Zuñiga, A. Encinas, J. Oliva, "Enhancing the capacitance and tailoring the discharge times of flexible graphene supercapacitors with cobalt ferrite nanoparticles", *Synth. Met.*, **264** (2020) 116384–116395.
8. Y.G. Wang, Z.D. Wang, Y.Y. Xia, "An asymmetric super-

- capacitor using RuO<sub>2</sub>/TiO<sub>2</sub> nanotube composite and activated carbon electrodes”, *Electrochim. Acta*, **50** (2005) 5641–5646.
9. S. Vijayakumar, S. Nagamuthu, G. Muralidharan, “Supercapacitor studies on NiO nanoflakes synthesized through a microwave route”, *ACS Appl. Mater. Interfaces*, **5** (2013) 2188–2196.
  10. M. Huang, F. Li, F. Dong, Y.X. Zhang, L.L. Zhang, “MnO<sub>2</sub>-based nanostructures for high-performance supercapacitors”, *J. Mater. Chem. A*, **3** (2015) 21380–21423.
  11. Eftekhari, L. Li, Y. Yang, “Polyaniline supercapacitors”, *J. Power Sources*, **3470** (2017) 86–107.
  12. B.M. Pires, W.G. Nunes, B.G. Freitas, F.E.R. Oliveira, V. Katic, C.B. Rodella, L.M. Silva, H. Zanin, “Characterization of porous cobalt hexacyanoferrate and activated carbon electrodes under dynamic polarization conditions in a sodium-ion pseudocapacitor”, *J. Energy Chem.*, **54** (2020) 53–62.
  13. Z. Liao, H.Y. Su, J. Cheng, G.T. Sun, L. Zhu, M.Q. Zhu, “CoFe<sub>2</sub>O<sub>4</sub>-mesoporous carbons derived from *Eucommia ulmoides* wood for supercapacitors: Comparison of two activation method and composite carbons material synthesis method”, *Ind. Crops. Prod.*, **171** (2021) 113861–113871.
  14. N.M. Farag, M.A. Deyab, A.M. El-Naggar, A.M. Aldhafiri, M.B. Mohamed, Z.K. Heiba, “Exploring the functional properties of CuCo<sub>2</sub>O<sub>4</sub>/CuS nanocomposite as improved material for supercapacitor electrode”, *J. Mater. Res. Technol.*, **10** (2021) 1415–1426.
  15. P. Liu, H. Chen, X. Chang, Y. Xue, J. Zhou, Z. Zhao, H. Lin, S. Han, “Novel method of preparing CoFe<sub>2</sub>O<sub>4</sub>/graphene by using steel rolling sludge for supercapacitor”, *Electrochim. Acta*, **231** (2017) 565–574.
  16. A.M. Elseman, M.G. Fayed, S.G. Mohamed, D.A. Rayan, N.K. Allam, M.M. Rashad, Q.L. Song, “CoFe<sub>2</sub>O<sub>4</sub>@carbon spheres electrode: A one-step solvothermal method for enhancing the electrochemical performance of hybrid supercapacitors”, *ChemElectroChem*, **7** (2020) 526–534.
  17. B. Rani, N.K. Sahu “Electrochemical properties of CoFe<sub>2</sub>O<sub>4</sub> nanoparticles and its rGO composite for supercapacitor”, *Diam. Relat. Mater.*, **108** (2020) 107978–107987.
  18. Z. Wang, W. Jia, M. Jiang, C. Chen, Y. Li, “One-step accurate synthesis of shell controllable CoFe<sub>2</sub>O<sub>4</sub> hollow microspheres as high-performance electrode materials in supercapacitor”, *Nano Res.*, **9** (2016) 2026–2033.
  19. T. Das, B. Verma, “High performance ternary polyaniline-acetylene black-cobalt ferrite hybrid system for supercapacitor electrodes”, *Synth. Met.*, **251** (2019) 65–74.
  20. C.B. Aquino, D.A. Nagaoka, M.M. Machado, E.G. Cândido, A.G.M. de Silva, P.H.C. Camargo, S.H. Domingues, “Chemical versus electrochemical: What is the best synthesis method to ternary GO/WO<sub>3</sub>NW/PAni nanocomposites to improve performance as supercapacitor?”, *Electrochim. Acta*, **356** (2020) 136786–136795.
  21. P. Xiong, H. Huang, X. Wang, “Design and synthesis of ternary cobalt ferrite/graphene/polyaniline hierarchical nanocomposites for high-performance supercapacitors”, *J. Power Sources*, **245** (2014) 937–946.
  22. T. Prabhakaran, J. Hemalatha, “Combustion synthesis and characterization of cobalt ferrite nanoparticles”, *Ceram. Int.*, **42** (2016) 14113–14120.
  23. S.K. Gore, S.S. Jadhav, V.V. Jadhav, S.M. Patangr, M. Naushad, R.S. Mane, K.H. Kim, “The structural and magnetic properties of dual phase cobalt ferrite”, *Sci. Rep.*, **7** (2017) 2524.
  24. M. Houshiar, F. Zebhi, Z.J. Razi, A. Alidoust, Z. Askari, “Synthesis of cobalt ferrite (CoFe<sub>2</sub>O<sub>4</sub>) nanoparticles using combustion, coprecipitation, and precipitation methods: A comparison study of size, structural, and magnetic properties”, *J. Magn. Magn. Mater.*, **371** (2014) 43–48.
  25. A.B. Salunkhe, V.M. Khot, M.R. Phadare, S.H. Pawar, “Combustion synthesis of cobalt ferrite nanoparticles - Influence of fuel to oxidizer ratio”, *J. Alloys Compd.*, **514** (2012) 91–96.
  26. S.H. Xiao, W.F. Jiang, L.Y. Li, X.J. Li, “Low-temperature auto-combustion synthesis and magnetic properties of cobalt ferrite nanopowder”, *Mater. Chem Phys.*, **106** (2007) 82–87.
  27. M.S. Khandekar, R.C. Kambale, J.Y. Patil, Y.D. Kolekar, S.S. Suryavanshi, “Effect of calcination temperature on the structural and electrical properties of cobalt ferrite synthesized by combustion method”, *J. Alloys Compd.*, **509** (2011) 1861–1865.
  28. C. Murugesan, M. Perumal, G. Chandrasekaran, “Structural, dielectric and magnetic properties of cobalt ferrite prepared using auto combustion and ceramic route”, *Phys. B Condens. Mat.*, **448** (2014) 53–56.
  29. A. Dandekar, R.T.K. Baker, M.A. Vannice, “Characterization of activated carbon, graphitized carbon fibers and synthetic diamond powder using TPD and DRIFTS”, *Carbon*, **36** (1998) 1821–1831.
  30. M. Karnan, K. Subramani, P.K. Srividhya, M. Stahish, “Electrochemical studies on corncob derived activated porous carbon for supercapacitors application in aqueous and non-aqueous electrolytes”, *Electrochim. Acta*, **228** (2017) 586–596.
  31. D. Qu, “Studies of the activated carbons used in double-layer supercapacitors”, *J. Power Sources*, **109** (2022) 403–411.
  32. K. Kaneko, C. Ishii, M. Ruike, H. Kuwabara, “Origin of superhigh surface area and microcrystalline graphitic structures of activated carbons”, *Carbon*, **30** (1992) 1075–1088.
  33. V.K. Gupta, I. Ali, T.A. Saleh, M.N. Siddiqui, S. Agarwal, “Chromium removal from water by activated carbon developed from waste rubber tires”, *Environ. Sci. Pollut. Res.*, **20** (2013) 1261–1268.
  34. L.M. da Silva, R. Cesar, C.M.R. Moreira, J.H.M. Santos, L.G. de Souza, B.M. Pires, R. Vicentini, W. Nunes, H. Zanin, “Reviewing the fundamentals of supercapacitors and the difficulties involving the analysis of the electrochemical findings obtained for porous electrode materials”, *Energy Storage Mater.*, **27** (2020) 555–590.
  35. R.S. Yadav, I. Kuritka, J. Vilcakova, J. Havlicka, L. Kalina, J. Tkacz, J. Švec, V. Enev, M. Hajdúchová, “Impact of grain size and structural changes on magnetic, dielectric, electrical, impedance and modulus spectroscopic characteristics of CoFe<sub>2</sub>O<sub>4</sub> nanoparticles synthesized by honey mediated sol-gel combustion method”, *Adv. Nat. Sci. Nanosci. Nanotechnol.*, **8** (2017) 045002.
  36. N. Shimodaira, A. Masui, “Raman spectroscopic investigations of activated carbon materials”, *J. Appl. Phys.*, **92** (2002) 902–909.
  37. B. Li, F. Dao, Q. Xiao, L. Yang, J. Shen, C. Zhang, M. Cai “Nitrogen-doped activated carbon for a high energy hybrid

- supercapacitor”, *Energy Environ. Sci.*, **9** (2016) 102–106.
38. S.M. Alshehri, J. Ahmed, A.N. Alhabarah, T. Ahamad, T. Ahmad, “Nitrogen-doped cobalt ferrite/carbon nanocomposites for supercapacitor applications”, *Chem. Electro. Chem.*, **4** (2017) 2952–2958.
39. R. Vicentini, R. Beraldo, J.P. Aguiar, F.E. Oliveira, F.C. Rufino, D.R.G. Larrude, L.M. da Silva, H. Zanin, “Niobium pentoxide nanoparticles decorated graphene as electrode material in aqueous-based supercapacitors: Accurate determination of the working voltage window and the analysis of the distributed capacitance in the time domain”, *J. Energy Storage*, **44** (2021) 103371–103385.
40. M. Cakici, K.R. Reddy, F. Alonso-Marroquin, “Advanced electrochemical energy storage supercapacitors based on the flexible carbon fiber fabric-coated with uniform coral-like MnO<sub>2</sub> structured electrodes”, *Chem. Eng. J.*, **309** (2017) 151–158.
41. S. Lalwani, R.B. Marichi, M. Mishra, G. Gupta, G. Singh, R.K. Sharma, “Edge enriched cobalt ferrite nanorods for symmetric/asymmetric supercapacitive charge storage”, *Electrochim. Acta*, **283** (2018) 708–717.
42. F. Barzegar, A.A. Khaleed, F.U. Ugbo, K.O. Oyeniran, D.Y. Momodu, A. Bello, J.K. Dangbegnon, N. Manyala, “Cycling and floating performance of symmetric supercapacitor derived from coconut shell biomass”, *AIP Adv.*, **6** (2016) 115306–115315.
43. K.V. Sankar, S. Shanmugapriya, S. Surendran, S.C. Jun, R.K. Selvan, “Facile hydrothermal synthesis of carbon-coated cobalt ferrite spherical nanoparticles as a potential negative electrode for flexible supercapattery”, *J. Colloid Interface Sci.*, **513** (2018) 480–488.
44. R. Vellacheri, A. Al-haddad, H. Zhao, W. Wang, C. Wang, Y. Lei, “High performance supercapacitor for efficient energy storage under extreme environmental temperatures”, *Nano Energy*, **8** (2014) 231–237.
45. E. Ellanthamilan, S. Rajkumar; J.P. Merlin, D.S. Jona, B.K. Monisha, B.C. Meena, “Effect of decorating cobalt ferrite spinel structures on pistachio vera shell-derived activated carbon on energy storage applications”, *Electrochim. Acta*, **359** (2020) 136953–136962.
46. M.M. Baig, I.H. Gul, “Transformation of wheat husk to 3D activated carbon/NiCo<sub>2</sub>S<sub>4</sub> frameworks for high-rate asymmetrical supercapacitors”, *J. Energy Storage*, **37** (2021) 102477.